Scavenger Receptor Mediated Endocytosis of Silver Nanoparticles into J774A.1 Macrophages Is Heterogeneous

Hongyun Wang, Linxi Wu, and Björn M. Reinhard*

Department of Chemistry and The Photonics Center, Boston University, Boston, Massachusetts 02215, United States

ABSTRACT

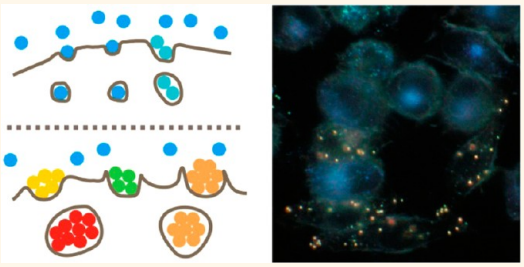

We investigated the scavenger receptor mediated uptake and subsequent intracellular spatial distribution and clustering of 57.7 ± 6.9 nm diameter silver nanoparticles (zeta-potential = −28.4 mV) in the murine macrophage cell line J774A.1 through colorimetric imaging. The NPs exhibited an overall red-shift of the plasmon resonance wavelength in the cell ensemble as function of time and concentration, indicative of intracellular NP agglomeration. A detailed analysis of the NP clustering in individual cells revealed a strong phenotypic variability in the intracellular NP organization on the single cell level. Throughout the observation time of 24h cells containing non- or low-agglomerated NPs with a characteristic blue color coexisted with cells containing NPs with varying degrees of agglomeration, as evinced by distinct spectral shifts of their resonance wavelengths. Pharmacological inhibition studies indicated that the observed differences in intracellular NP organization resulted from coexisting actin- and clathrin-dependent endocytosis mechanisms in the macrophage population. Correlation of intracellular NP clustering with macrophage maturity marker (F4/80, CD14) expression revealed that differentiated J774A.1 cells preferentially contained compact NP agglomerates, whereas monocyte-like macrophages contained non-agglomerated NPs.

KEYWORDS: plasmon coupling microscopy · nanotoxicology · nanoparticle endocytosis · nanoparticle trafficking · macrophage maturation · ensemble heterogeneity

Nanotechnology seeks to utilize the unique physicochemical properties of materials on the 1−100 nm length scale in a diverse range of applications. Nanoparticles (NPs) are important building blocks of this emerging technology, and although their applications in consumer products are rapidly increasing, the current understanding of potential risks associated with the release of these materials in the environment for human and animal health is still insufficient.[1−4] This knowledge gap motivates fundamental studies into the intricate interactions between cellular systems and NPs. In this work we focus on the scavenger receptor mediated uptake and subsequent trafficking of silver NPs in the adherent mouse macrophage cell line J774A.1. Macrophages belong to the mononuclear phagocyte system (MPS),[5] which plays a prominent role in the clearing of environmental microparticles or microorganisms from the body. Macrophages are equipped with a broad range of pattern recognition receptors that enable the cell to recognize unopsinized objects with specific surface features, which the body commonly associates with pathogens or debris.[6] Since macrophages are "first responders" to all foreign materials, including NPs, mature *in vitro* murine macrophage cell lines, such as J774A.1, are commonly used model systems for studying various aspects of NP uptake and the potentially related toxicity under well-defined environmental conditions.[7−16]

Scavenger receptors are a subgroup of pattern recognition receptors that recognize negative surfaces and are known to trigger the internalization of micrometer-sized exogenous and endogenous objects, such as apoptotic cells, bacteria, and dust particles through phagocytosis.[17] There is increasing experimental evidence that scavenger receptors also recognize nanoscale objects, including engineered NPs.[18−20] In fact, clathrin-dependent, scavenger receptor A mediated endocytosis was found to be the major uptake mechanism for carboxydextran-coated (and thus negatively charged) iron oxide NPs with diameters of 20 and 60 nm in human macrophages.[21] Scavenger receptor mediated NP uptake comprises three fundamental stages: (i) NP binding, (ii) NP internalization, and (iii) intracellular transport and redistribution. Together these processes result in a spatial

* Address correspondence to bmr@bu.edu.

Received for review May 17, 2012 and accepted July 16, 2012.

Published online July 16, 2012
10.1021/nn302186n

translocation of NPs from the extracellular space through the membrane toward special processing centers within the cell. Endocytosis is, however, not a single defined mechanism; instead multiple uptake mechanisms coexist and are coupled to various vesicle trafficking mechanisms.[22,23] Given this complexity, it is hardly surprising that many aspects of the endocytosis of metal NPs into macrophages,[7,16,21,24,25] including the exact nature of the underlying cellular mechanisms and their dependence on the size, shape, and surface properties of the NPs, as well as the intracellular fate of the nondegradable NPs and their impact on the cell physiology, still pose important questions. Cell–nanoparticle interactions in biological media are complex since proteins, enzymes, or various small molecules can nonspecifically adsorb to the NP surface to form a corona.[26,27] The latter can modify the intracellular uptake and distribution of the NPs.

We focus in this work on the scavenger receptor mediated endocytosis of silver NPs since these particles are a cause for acute concern due to their already widespread use as antimicrobial agents in consumer products and medical devices.[28–31] Furthermore, silver NPs have superb photophysical properties and large optical scattering cross sections in the blue,[32–34] which makes the observation of their fate amenable in a conventional optical microscope.[34] The optical response of silver NPs is dominated by resonant electron density oscillations in the particles, which are referred to as plasmons.[35] The distance-dependent electromagnetic coupling[36,37] between plasmons in individual silver NPs provides a unique approach for monitoring the association of NPs into clusters during NP internalization and subsequent trafficking in real time.[38–43] If two particles approach each other to within approximately one particle diameter, their plasmons hybridize[44] and the coupled resonance red-shifts with decreasing interparticle separation.[36] If additional NPs attach to the dimer to form a larger cluster, the spectra further red-shift and broaden with growing number of NPs in the cluster. The ability to track NPs within cells and to simultaneously determine their association levels using plasmon coupling microscopy[38–40,45] provides exciting new opportunities for monitoring the spatiotemporal distribution of NPs in living cells. For J774A.1 cells our studies show that NP uptake leads to an agglomeration of the NPs on the ensemble level, but that the degree of NP clustering varies significantly between individual macrophages due to different NP endocytosis and processing strategies within the cell population.

RESULTS AND DISCUSSION

Verification of Scavenger Receptor Mediated Endocytosis. The silver NPs used in this work had a diameter of 57.7 ± 6.9 nm and were stabilized by assembling a monolayer of short polyethylene glycols (PEGs) functionalized with thiol and carboxylic acid residues at opposing ends onto the silver surface (see Methods). The resulting NPs had a zeta-potential of −28.4 mV and were stable against agglomeration in Hanks buffer containing Mg^{2+} and Ca^{2+} (HBSS). J774A.1 macrophages adherent to a glass slide were exposed to solutions of silver NPs of varying loading concentrations in HBSS buffer for 5 min at 37 °C. Subsequently, the NP solution was removed and the cells were washed with copious amounts of buffer and then cultured in a CO_2 incubator at 37 °C for defined times before inspection. We limited the incubation times of the NPs with the cells (i) to minimize contamination of the NP surface with opsonins or other ligands,[46] which could trigger NP uptake through specific receptors (other than scavenger receptors), and (ii) to track NP uptake and intracellular trafficking along a defined synchronized time axis in a process that is not complicated by further continuous uptake of additional NPs.

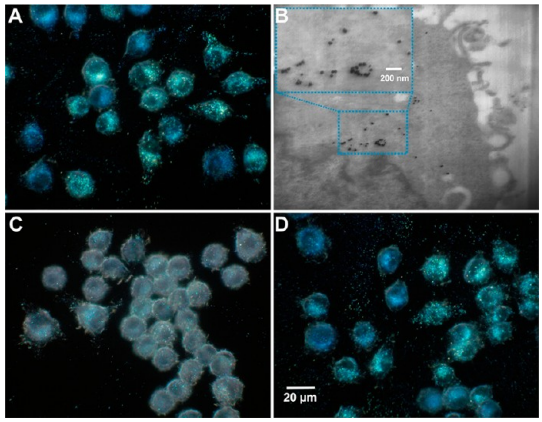

Figure 1. Silver NP uptake into J774A.1 macrophages is scavenger receptor mediated. (A) Dark-field image of a cluster of macrophages exposed to a 4.5 μg/mL solution of 57.7 nm Ag NP in HBSS for 5 min and then incubated in growth medium for 0.5 h. (B) TEM image of a macrophage section that shows clearly that the NPs are taken up into the cell interior. (C) Preincubation of the cells with 100 μg/mL poly-I blocks NP uptake. The macrophages were incubated with poly-I and then exposed to silver NP under identical conditions to those in A. (D) Preincubation of the cells with 100 μg/mL poly-C does not influence NP uptake.

In a first control experiment, we verified that silver NPs are taken up by J774A.1 macrophages and that the binding and uptake are scavenger receptor mediated. In Figure 1A we show a dark-field image of macrophages acquired 0.5 h after the initial exposure to a solution of 4.5 μg/mL silver NPs. The intense blue-green color indicates an efficient binding and subsequent uptake of NPs into the macrophage. The transmission electron microscope (TEM) image of a representative macrophage section obtained under these conditions in Figure 1B confirms NPs and NP clusters located in the cytoplasm of the macrophage. Preincubation of the cells with the

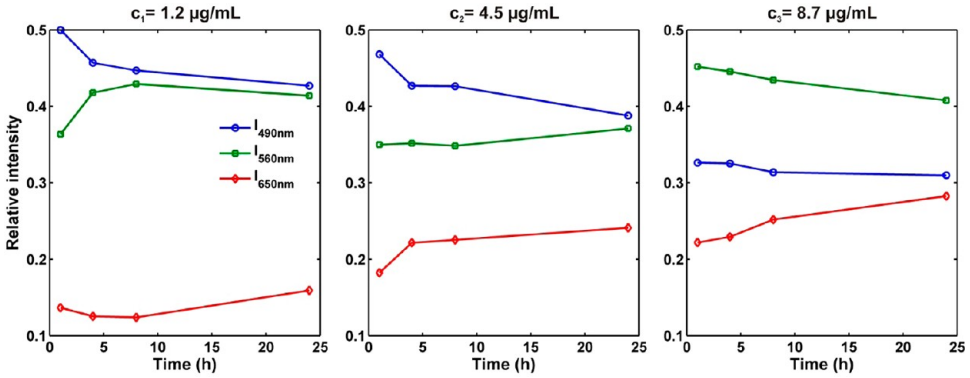

Figure 2. The plasmon resonance wavelength of silver NPs red-shifts as a function of NP concentration and time. Relative intensities of the light detected from silver NPs on three different wavelength channels (λ_1 = 490 nm (blue); λ_2 = 560 nm (green); λ_3 = 650 nm (red)). At t = 0 h the macrophages were exposed to solutions of silver NPs with concentrations of c_1 =1.2 μg/mL, c_2 = 4.5 μg/mL, and c_3 = 8.7 μg/mL for 5 min. After that, the cells were incubated in growth medium at 37 °C. We recorded data points at t = 1 h, 4 h, 8 h, and 24 h; 120−260 cells were evaluated per time point.

strongly negatively charged polymer polyinosinic acid (poly-I) almost completely inhibited NP binding (Figure 1C), whereas polycytidylic acid (poly-C) did not have a similar effect (Figure 1D). The selective inhibition of NP binding through poly-I is a characteristic sign of scavenger receptor mediated NP binding.[47]

Time and Concentration Dependence of NP Uptake and Intracellular Clustering. Noble metal NPs are a unique "cargo" for uptake studies since their scattering spectra encode information about their association state, enabling the tracking of their clustering state as function of location and time through optical microscopy.[38,41,45] This is highly relevant for elucidating the mechanisms underlying receptor-mediated endocytosis of NPs since some studies have shown that the uptake is strongly size dependent and can require a clustering of NPs on the plasma membrane.[48−54] Furthermore, scavenger receptor mediated endocytosis involves the incorporation of NPs into vesicles at the plasma membrane. These vesicles are expected to fuse with other membranes and endosomal compartments during their subsequent intracellular trafficking, which can result in a local enrichment of NPs in a confined space and, thus, induce agglomeration.[55]

In a first set of experiments we investigated the time and concentration dependence of NP clustering during scavenger receptor mediated endocytosis. We exposed the macrophages to three different concentrations of silver NPs in HBSS buffer (c_1 = 1.2 μg/mL, c_2 = 4.5 μg/mL, c_3 = 8.7 μg/mL) and then monitored for spectral shifts of the NPs at t = 1 h, 4 h, 8 h, and 24 h by analyzing the intensity distribution of the scattered light on three wavelength channels ($\lambda_1 = 490 \pm 20$ nm, $\lambda_2 = 560 \pm 14$ nm, $\lambda_3 = 650 \pm 10$ nm). We used a total intensity threshold to identify the NP-containing areas in the recorded cell image and then determined the contribution from λ_1−λ_3 in the identified image areas (see Methods). For each concentration and time point we evaluated at least 120 individual cells. Figure 2 summarizes the resulting ensemble-averaged intensity distributions as function of time for the investigated NP concentrations.

For c_1 the λ_1 channel dominates the scattering spectra at t = 1 h, but its contribution continuously decreases as a function of time, whereas the contribution from λ_2 overall increases. Between t = 8 h and t = 24 h the intensity in the λ_3 channel also slightly increases. For cells that were exposed to a solution of silver NPs of concentration c_2, λ_1 still represents the major contribution to the NP spectrum at t = 1 h, but its intensity is lower than for c_1. The decrease in intensity of the λ_1 channel at t = 1 h is accompanied by an increase in the scattering intensity on the λ_3 channel. With increasing time, the intensity of λ_1 further decreases, whereas λ_3 increases. The intensity of λ_2 remains nearly constant over time; only between t = 8 h and t = 24 h have we observed a small increase in λ_2. For the highest investigated NP concentration, c_3, the spectra are much more red-shifted than for c_1 and c_2. The intensity in the λ_2 channel is already dominating at t = 1 h. With increasing time the intensities for λ_2 and λ_1 decrease and the intensity for λ_3 increases.

The above analysis reveals a clear red-shift of the average plasmon resonance wavelength as a function of time for all three investigated NP concentrations. This finding is consistent with a gradual clustering of the NPs during the uptake and subsequent intracellular trafficking. The comparison of the three panels in Figure 2 also shows that the resonance wavelengths evaluated at a constant time red-shift with increasing concentration of the initial NP loading solution, confirming a concentration dependence of the association process.

Heterogeneity in NP Uptake and Association. Although the ensemble-averaged resonance wavelength shows a general red-shift as a function of both NP concentration (c_i) and time, the optical inspection of individual cells one and eight hours after exposure to c_i (Figure 3) reveals significant cell-to-cell differences in the color (and thus association state) of the ingested NPs. In the case of c_1 we find macrophages that contain vividly

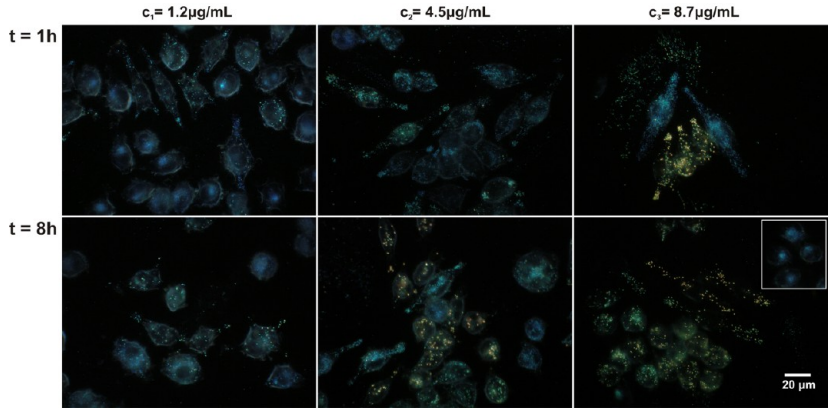

Figure 3. The NP association of silver NPs in J774A.1 cells is heterogeneous. Representative dark-field images of J774A.1 macrophages exposed to silver NP solutions with concentrations of c_1 = 1.2 μg/mL, c_2 = 4.5 μg/mL, and c_3 = 8.7 μg/mL for 5 min. The images were acquired after incubation in a particle-free culture medium for t = 1 h and 8 h at 37 °C. The difference in the color between individual cells indicates systematic variations in NP association levels due to phenotypic variations in NP uptake and/or processing. The inset for c_3, t = 8 h shows that even after exposure to a high concentration of NPs and incubation for several hours, some cells still contain exclusively NPs with scattering resonances in the blue.

blue NPs besides cells containing bluish-green NPs at both t = 1 h and 8 h. A detail of special note is that in many cells containing primarily blue NPs these particles are often confined to diffuse intracellular compartments. For c_2 we observe more frequently cells that contain NPs of green color distributed across the entire cytoplasm at t = 1 h, which is indicative of small- to medium-sized NP agglomerates. These cells coexist with cells that still contain primarily blue NPs. At t = 8 h, the number of cells containing large NP clusters with orange-yellow color has increased, but cells containing only blue NPs are still frequent. If the loading concentration is further increased to c_3, we observe numerous cells with compact orange NP agglomerates already at t = 1 h. But as observed for c_1 and c_2, the cells of the ensemble do not show a uniform NP association level, and macrophages containing non- or low-agglomerated NPs with a strong spectral response in the blue are still present. At t = 8 h NP agglomeration is advanced in many cells, but significant color differences between individual cells remain. Even cells containing exclusively blue NPs (see inset for (c_3, t = 8 h) in Figure 3) can still be identified.

The optical inspection of macrophages after NP exposure indicates a broad range of phenotypic variability in NP uptake and intracellular processing. This conclusion is further corroborated by monitoring NP association in individual macrophages in real time (Figure 4). Whereas the macrophage in Figure 4A does not show any significant NP agglomeration in the monitored time window of 15−45 min, the macrophage in Figure 4B exhibits an increase in yellow-orange scatterers, which confirms a redistribution of NPs within the macrophage.

The prolonged existence of cells containing vividly blue NPs in Figure 3 is especially remarkable. To ensure that these NPs were indeed taken up and not just adherent to the cells, we combined plasmon coupling

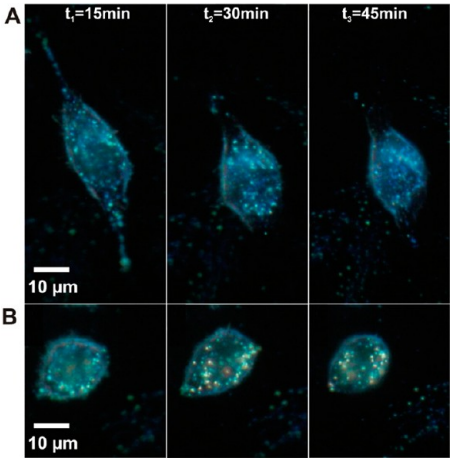

Figure 4. Real-time monitoring of NP association reveals differences in NP processing in individual macrophages. While the macrophage in A does not show a systematic increase of NP agglomeration, an increase in the number of yellow-orange scatterers, indicative of agglomeration, is observed for the macrophage in B. The cells were first incubated with a NP concentration of c_2 = 4.5 μg/mL, cleaned in prewashed HBSS buffer, and transferred into the optical microscope, where the tracking experiments were performed at 37 °C. The given time stamps specify the incubation time in NP-free medium.

microscopy with conventional fluorescence microscopy to check for co-localization of the NPs inside the cells with endosomal compartments. We analyzed cells initially exposed to silver NPs of concentration c_3 after incubation for t = 24 h. Figure 5A shows a representative dark-field image, and Figure 5B shows the corresponding fluorescence image after staining with LysoTracker Red, which is fluorescent only in strongly acidic compartments, such as the lysosome. The compartments containing blue NPs co-localize well with the lysosome marker, confirming that the NPs have indeed been translocated into the cell interior through a vesicular trafficking process.

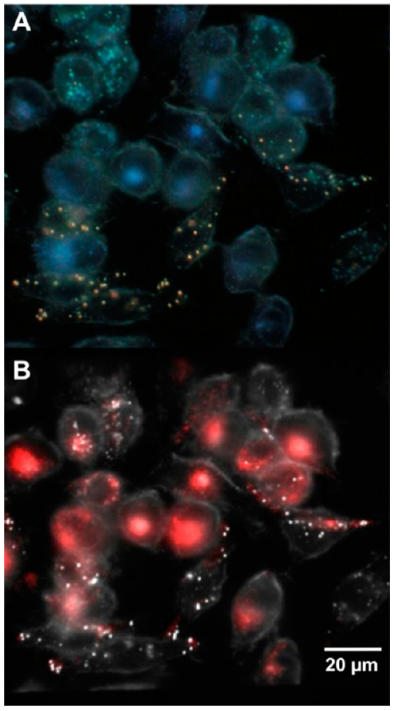

Figure 5. Correlation of dark-field and fluorescence microscopy after treatment with LysoTracker Red. (A) Color dark-field image. (B) Monochromatic dark-field image with overlaid fluorescence image. Blue-shaded cell regions containing an enrichment in NPs strongly co-localize with the lysosome tracker.

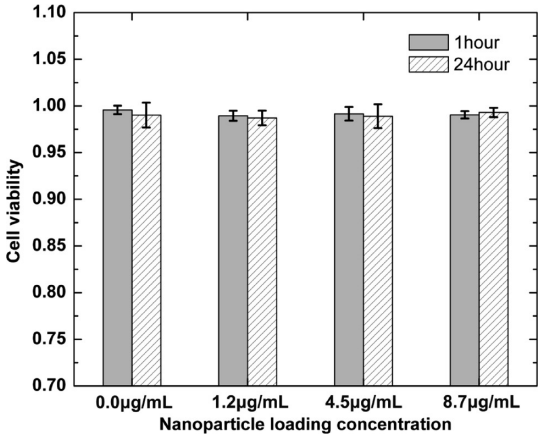

Figure 6. Silver NP uptake does not affect cell viability. The histogram shows the cell viabilities obtained after exposing macrophages to NP concentrations of 0.0 μg/mL, c_1 = 1.2 μg/mL, c_2 = 4.5 μg/mL, and c_3 = 8.7 μg/mL for 5 min and subsequent incubation for 1 or 24 h, respectively.

Overall, our optical studies show that NPs are efficiently taken up by the macrophages and that the exact intracellular distribution of the NP varies substantially between individual cells, indicative of significant variability in the uptake and processing mechanisms in different cells.

Cytotoxicity of the Silver NPs. We monitored the influence of silver NPs on the viability of the macrophages using a live/dead assay (see Methods), t = 1 h and t = 24 h, after exposure to silver NPs for 5 min. We did not observe any systematic decrease in cell viability for the NP concentration range of relevance in this work (Figure 6). We conclude that under the chosen experimental conditions the effect of the silver NPs and of potentially released silver ions[56,57] on the cell viability is low. On the basis of this data we exclude silver nanoparticle induced toxicity as a source for the heterogeneity observed in the intracellular NP organization.

Probing NP Uptake Mechanisms through Pharmacological Inhibitors. Our studies show that the silver NPs used in this work bind to scavenger receptors on J774A.1 cells and are subsequently taken up into the cell interior. In this section we will characterize the uptake process in further detail by determining the contributions from different endocytosis mechanisms. In a first set of experiments we checked for passive translocation of NPs across the membrane at 4 °C under otherwise identical conditions as before. At 4 °C all active endocytosis is stalled, and we did not detect any indications of NP uptake. Instead, the total scattering intensity of the cells was significantly lower than for experiments performed at 37 °C, and NPs were exclusively detected attached to the apical cell surface. These observations confirm that the NP uptake is the result of energy-dependent endocytosis.

TABLE 1. Summary of the Pharmacological Inhibitors Used and Their Functions

inhibition chemicals	functions
monodansyl cadaverine	inhibits transamidase activity and clathrin-coated pit formation[71]
chlorpromazine	blocks clathrin disassembly and recycling[72]
amantadine	blocks the budding of clathrin-coated pits[73]
nystatin	disrupts lipid-raft[74]
genistein	inhibits the phosphorylation of caveolin[75]
methyl-β-cyclodextrin	sequesters cholesterol from the membrane[74]
colchincine	depolymerizes microtubles[76]
rottlerin	inhibits protein kinase C[77]
wortmannin	inhibits phosphatidylinositol (PI)-3-kinase[78]
cytochalasin B	depolymerizes actin microfilament[71]
cytochalasin D	depolymerizes actin microfilament[79]

In the next step, we systematically blocked various endocytosis pathways using pharmacological inhibitors. An overview of the applied pharmacological inhibitors and the affected uptake mechanisms is given in Table 1. We verified in control experiments with selected reagents (see Methods) that the inhibitors efficiently affected the internalization of positive controls under the chosen experimental conditions. In the case of NPs we detected unequivocal deviations from noninhibited uptake in the association and spatial distribution of NPs only for inhibitors that affect clathrin-mediated or actin-dependent endocytosis. Figure 7 shows representative dark-field images of the cells obtained under these conditions using c_2= 4.5 μg/mL and an incubation time of 1 h. When the

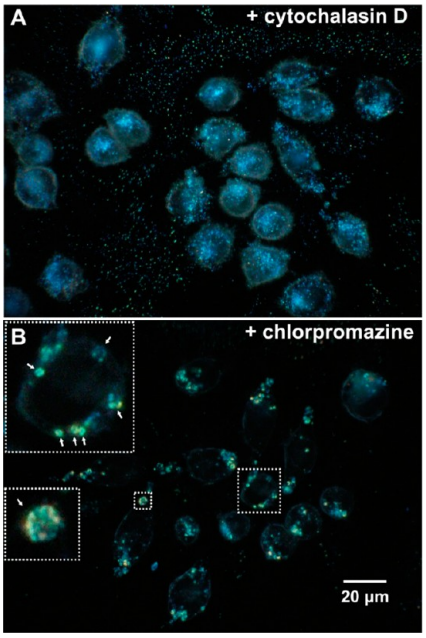

Figure 7. Pharmacological inhibitors indicate that clathrin-dependent and actin-dependent endocytosis processes participate in silver NP uptake. (A) In the presence of cytochalasin D (blocks actin-dependent endocytosis) only the blue macrophage phenotype is observed. (B) Treatment with chlorpromazine (blocks clathrin-dependent endocytosis) leads to the formation of large NP agglomerates in spatially defined compartments, some of which are magnified in the insets.

actin-mediated endocytosis of NPs was inhibited by cytochalasin D, we exclusively observed the "blue" cell phenotype (Figure 7A). NP agglomerates with a red-shifted spectral response were absent, indicating that the formation of larger NP agglomerates is actin-dependent. In contrast, the inhibition of clathrin-mediated endocytosis (Figure 7B) led to an overall decrease in the amount of NPs with a spectral response in the blue. NP agglomerates were also present, but the intracellular distribution of the NPs and clusters changed. Especially in the presence of chlorpromazine, the NPs were often found to be concentrated in specific subcellular compartments with prominent concentric, "doughnut"-like shapes, which were absent without inhibition. These compartments were found to be acidic using the pH-sensitive fluorescence dye LysoTracker Red. We conclude that although the inhibition of clathrin recycling through chlorpromazine did not inhibit the formation of intracellular NP agglomerates, the observed change in the spatial distribution of the NP agglomerates within the cells suggests some interplay of clathrin- and actin-based endocytosis machineries in the formation of NP agglomerates under uninhibited conditions.[58,59]

Interestingly, we found that cytochalasin D also induces significant changes in the spatial distribution of the NPs on the macrophage surface as determined by scanning electron microscopy. Figure 8 displays representative SEM images of cells after exposure to

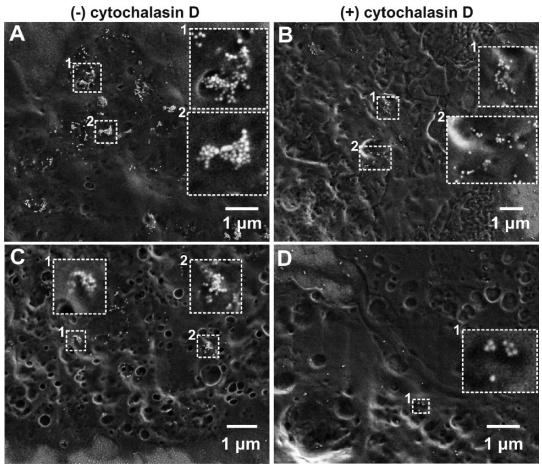

Figure 8. Cytochalasin D reduces NP clustering on the macrophage cell surface. After exposure to a 4.5 μg/mL nanoparticle solution for 5 min, the cells were cultured for 20 min before fixation and inspection in the SEM. Left column: SEM images of macrophages obtained in the absence of cytochalasin D. Representative images for high (A) and low (C) NP density are shown. Right column: SEM images obtained in the presence of 10 μg/mL cytochalasin D. Representative images for high (B) and low (D) NP density are shown. Only in the absence of cytochalasin D are large NP clusters observed. Selected areas are magnified in the insets. All scale bars represent 1 μm.

a loading solution of 4.5 μg/mL for 5 min and subsequent incubation in NP-free culture medium for 20 min with and without cytochalasin D. Top and bottom rows show representative SEM images of high and low NP association levels, respectively, for both conditions. Whereas in the absence of cytochalasin D (Figure 8A and C) we frequently detected large NP clusters on the cell surface, the NP association on the cell surface was much less prominent for cytochalasin D-treated cells (Figure 8B and D). One possible interpretation of the differences in NP clustering observed in our optical and electron microscopic studies is the existence of two uptake mechanisms. In the first mechanism individual 57.7 nm diameter NPs and small NP clusters are directly taken up *via* a clathrin-dependent but actin-independent pathway, which avoids an accumulation of NPs on the cell surface, whereas a second actin-dependent mechanism involves the association of NPs into larger clusters on the cell surface. Similar to conventional phagocytosis the surface-formed NP clusters are finally engulfed in an actin-dependent step. Although the two identified endocytosis mechanisms coexist in the macrophage ensemble, our data indicate that—in the absence of inhibitors—the two mechanisms are mutually exclusive in individual cells.

Correlating NP Processing with F4/80 and CD14 Surface Antigen Expression. Macrophages mature from monocytes and can develop diverse dynamic phenotypes depending on their environment.[60−62] Detailed phenotyping of J774A.1 macrophages has revealed that

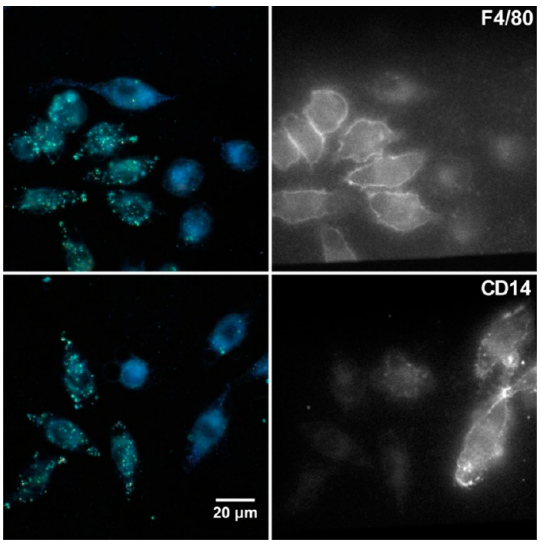

Figure 9. Phenotypic variations in NP uptake are correlated with F4/80 and CD14 expression levels. Left: Dark-field image of macrophages with silver NPs ($c_2 = 4.5$ μg/mL, $t = 4$ h). Right: Corresponding fluorescence image labeled for F4/80 (top) or CD14 (bottom). Macrophages containing NPs with blue color show low F4/80 intensity and high CD14 intensity, whereas macrophages containing NP agglomerates, as indicated by their green color, show high F4/80 and low CD14 intensity.

these cells are at an intermediate stage of development between monocytes and macrophages.[63,64] An inspection of the cells in Figure 3 shows that the J774A.1 cell population is heterogeneous with regard to the morphology of the individual cells. Some cells are round and compact, whereas others are stretched and elongated. The observation of this morphological heterogeneity is consistent with the findings of previous studies and indicates different differentiation states within the cell culture.[60,65,66] We wondered whether the observed heterogeneity in the silver NP uptake and processing observed in this study is correlated with different macrophage differentiation states. To test this hypothesis, we augmented the colorimetric information about the NP aggregation obtained from dark-field microscopy with relative measures of the macrophage maturity markers CD14 and F4/80 as obtained through fluorescence immunostaining. While F4/80 is characteristic of mature macrophages,[67] CD14 is preferentially expressed by less differentiated monocytes.[61,62]

We performed the experiments in an identical fashion to that described before for monitoring the NP uptake but limited our analysis to one silver NP concentration (c_2) and incubation time (t = 4 h). Figure 9 shows correlated dark-field and fluorescence images for macrophages with labeled F4/80 (top row) or CD14 (bottom row) obtained under these conditions. The representative images show that cells containing a higher degree of NP agglomeration (*i.e.*, that have green or orange color) show higher expression levels of F4/80, whereas the cells containing nonclustered NPs (*i.e.*, that are blue) show higher expression levels of CD14. These findings confirm that one important parameter that contributes to the phenotypic variability with regard to the NP processing is the maturation state of the macrophages. Taking into account the results of our endocytosis inhibition studies, we can conclude that scavenger receptor mediated NP uptake by differentiated J774A.1 macrophages is associated with the formation of NP clusters through the described actin-dependent endocytosis process, whereas monocyte-like J774A.1 cells contain smaller NP agglomerates or even individual NPs, taken up through the clathrin-dependent but actin-independent endocytosis. This behavior is overall consistent with the general trend observed for the internalization of larger objects that mature macrophages show a more effective phagocytosis than monocytes.[68−70]

CONCLUSION

Due to their superb photophysical properties and their clustering-dependent spectral responses, silver NPs facilitate a direct quantitative optical tracking of their uptake and intracellular fate. In this article we investigated the interactions of negatively charged silver NPs with J774A.1 murine macrophages under sufficiently low NP concentrations to avoid a measurable impact on cell viability. Our findings demonstrate that the uptake of the silver NPs is mediated by scavenger receptors, which enable an efficient binding of the NPs to the macrophage surface. Furthermore, ensemble-averaged spectral characterizations of the NPs confirmed that their internalization is associated with a time- and concentration-dependent association into NP clusters. A more detailed investigation of the NP association patterns on the single cell level revealed dramatic cell-to-cell fluctuations in the spatial clustering of the NPs within the cells. We characterized the internalization of the NPs using pharmacological inhibitors and found indications of two coexisting uptake mechanisms: actin- and clathrin-dependent endocytosis. The clathrin-dependent endocytosis leads to nonagglomerated NPs within the cells with a strong spectral response in the blue, while actin-dependent endocytosis leads to the formation of compact NP clusters whose spectral responses are significantly red-shifted. The NP organization on the macrophage surfaces, as characterized in the SEM, indicates that the actin-dependent uptake involves NP clustering on the cell surface. Pronounced differences in the expression of macrophage maturity markers imply that the nonagglomerated NP phenotype is preferentially associated with monocyte-like J774A.1 cells, while the NPs in more mature macrophages show a higher degree of aggregation.

The observed heterogeneities in NP uptake and processing are important, since J774A.1 is a commonly

used model system for the nanotoxicological characterization of engineered NPs. Our findings suggest that an explicit consideration of the heterogeneity in the nanoparticle−cell interactions can further improve the reliability of nanotoxicological predictions obtained *in vitro* with J774A.1 and other macrophage cell lines.

METHODS

Nanoparticle Preparation and Characterization. Citrate-stabilized silver NPs from British Biocell International (Ted Pella, catalog number 15707-1SC) were used for all experiments. The average diameter of the NPs, as determined by TEM, was 57.7 ± 6.9 nm, and the average aspect ratio was 1.17 ± 0.15. TEM images and size and shape distributions of the NPs are shown in Figure S1. The TEM image confirms that the NPs were roughly spherical and had a smooth surface. The citrate ligands were exchanged with PEGs by incubating the NPs overnight in a 10 mM aqueous solution of (HS-$(CH_2)_{11}$-$(OCH_2CH_2)_6$-OCH_2-COOH), then washed by centrifugation and resuspended in HBSS buffer (137.93 mM NaCl, 5.33 mM KCl, 4.17 mM $NaHCO_3$, 0.441 mM KH_2PO_4, 0.338 mM Na_2HPO_4, 0.407 mM $MgSO_4$, 0.493 mM $MgCl_2$, 1.26 mM $CaCl_2$, 5.56 mM D-glucose) before incubation with the cells. UV−vis spectra of the NP solution acquired before and after incubation with the cells indicated that the PEG-functionalized NPs were stable (Figure S2). Zeta-potential measurements of PEG-functionalized NPs in water were performed using a Malvern NANO-ZS90 Zetasizer at 25 °C.

Cell Culturing. The murine macrophage J774A.1 cell line was purchased from American Type Culture Collection. The cells were cultured in advanced Dulbecco's modified Eagle medium (DMEM) supplemented with 10% fetal bovine serum, 2 mM L-glutamine, 50 units/mL penicillin, and 50 μg/mL streptomycin in an incubator at 37 °C, 5% CO_2, and 95% relative humidity. To subculture, cells were detached from the flask substrate by gentle scraping, aspirated, and dispensed into fresh complete culture medium. Cells to be imaged under dark-field microscopy or fluorescence microscopy were grown on glass coverslides to approximately 30% confluency.

Monitoring NP Uptake. A glass slide containing adherent macrophages was covered by 0.5 mL of NP-containing solution (c = 1.2−8.7 μg/mL) in HBSS buffer and incubated for 5 min at 37 °C. Then the cells were washed with prewarmed HBSS buffer, and the NP-containing solution was replaced by culture medium. The cells were then incubated for variable periods of time (t = 1−24 h) before optical characterization with the dark-field microscope equipped with a cage incubator.

Effect of Homopolymeric Nucleic Acids on Nanoparticle Uptake. Cells were preincubated with 100 μg/mL polyinosinic acid or 100 μg/mL polycytidylic acid containing culture medium for 0.5 h and then incubated with a solution of 4.5 μg/mL silver NPs in HBSS buffer that contained identical amounts of either of poly-I or poly-C for 5 min. After the slides containing the cells were rinsed with HBSS, the cells were cultured for another 0.5 h in the poly-I- or poly-C-containing medium. Finally the slides containing cells were integrated into a homemade chamber and transferred to an optical microscope for inspection. Images were recorded under dark-field white-light illumination. Control slides were treated in an identical fashion, but addition of poly-I and poly-C was omitted.

Pharmacological Inhibition of NP Uptake. Macrophage cells (J774A.1) were preincubated with different pharmacological pathway inhibitors at 37 °C (clathrin-mediated endocytosis: 200 μM monodansyl cadeverine for 20 min, 10 μg/mL chlorpromazine for 1 h, 500 μM amantadine for 0.5 h; caveolae/lipid raft-mediated endocytosis: 200 μM genistein for 1 h, 50 μg/mL nystatin for 15 min, 2.5 mM methyl-beta-cyclodextrin (MβCD) for 2 h; pinocytosis: 10 μg/mL colchicine for 0.5 h; macropinocytosis, 2 μM rottlerin for 0.5 h; fluid-phase endocytosis, 400 nM wortmannin for 0.5 h; phagocytosis and macropinocytosis: 10 μg/mL cytochalasin B for 2 h, 10 μg/mL of cytochalasin D for 2 h), then incubated with a prewarmed solution of 4.5 μg/mL NPs in inhibitor-containing HBSS buffer for 5 min. Subsequently, the unbound particles were washed away with copious amounts of prewarmed HBSS buffer, and cells were cultured for another 1 h in DMEM supplemented with the same amount of inhibitors before optical inspection.

The experimental conditions for the inhibition studies were based on published procedures, and for selected inhibitors for which reliable positive controls were available we validated the efficacy in internalization assays. Alexa-Fluor 488-Transferrin (Life Technologies), FITC-Dextran (Life Technologies), and 1 μm polystyrene beads (Sigma-Aldrich) were used as markers for the clathrin-mediated pathway, fluid-phase endocytosis, and phagocytosis. The control experiments (Figures S3 and S4) confirmed that the inhibitors efficiently block the uptake of the positive controls under the chosen experimental conditions.

TEM Sample Preparation. Cells grown on the culture flask were treated with 4.5 μg/mL Ag particles in HBSS for 5 min and then cultured in particle-free medium for 4 h. Then the cells were scraped off, suspended, washed with HBSS, and fixed with 2.5% glutaraldehyde in 1× PBS (pH = 7.4) for 1 h at room temperature. After washing three times with PBS for 10 min each time, the cells were postfixed with 1% OsO_4 for 0.5 h in the dark. Then the cells were further washed three times with 3.6% NaCl for 5 min each time, rinsed with distilled water for 5 min, and stained *en bloc* with 5% uranyl acetate for 1 h. After washing with distilled water, the cells were dehydrated in an ascending ethanol series (50%, 75%, 90%, 100%) and finally embedded in EMbed 812 (Electron Microscopy Sciences, Hatfield, PA, USA). Blocks were polymerized, sectioned, and mounted on copper grids. The grids were allowed to dry and imaged on a JEM2010 transmission electron microscope (JEOL Co., Peabody, MA, USA).

SEM Sample Preparation. The cell culture, nanoparticle treatment procedure, and pharmacological inhibitor treatment procedure were identical to sample preparation for the optical studies with the exception that the J774A.1 cells were grown on a 1 × 1 cm silicon substrate under the same culturing conditions. The cells on silicon substrates were fixed by 4% formaldehyde solution for 15 min under room temperature followed by three washings with ice-cold 1× PBS, each for 5 min. The substrates were rinsed with DI water and gently air-dried before inspected with a Zeiss SUPRA 40VP SEM using an acceleration voltage of 1.5 kV.

Dark-Field Microscopy. The cell slides were imaged in an inverted microscope (Olympus IX71) under dark-field illumination through a high numerical aperture (NA) oil condenser (NA = 1.2−1.4). The illumination light was provided by a 100 W xenon lamp (Till Oligochrome), which enabled rapid interchange between three different excitation filters (λ_1 = 494 ± 20 nm; λ_2 = 560 ± 14 nm; λ_3 = 650 ± 10 nm) and white-light excitation. The scattering light was collected through a 60× oil objective (NA = 0.65) and captured on an electron multiplying CCD (EMCCD, Andor Ixon$^+$). The light source and EMCCD were synchronized by a digital delay generator (Stanford Research System, model DG 645). The exposure time for each monochromatic image was 0.05 s, and the cycle time for a full set of four images was 0.4 s. Digital color images were recorded under white-light illumination using an Olympus SP310 digital camera attached to the microscope through an eyepiece adapter.

Colorimetric Imaging and Image Analysis. All image processing was performed with custom-written Matlab codes. The white-light and corresponding monochromatic images recorded in the three wavelength channels (λ_1, λ_2, λ_3) were background corrected (pixel-by-pixel) with the average pixel intensity calculated from cell-free regions of the same image. Subsequently, the monochromatic images were corrected for differences in the lamp intensity in (λ_1, λ_2, λ_3). After the cells had been localized in the white-light image, the intensity in the white-light image (I_w) and in the three monitored wavelength channels was determined for each pixel within the detected cell

areas. If I_w lay above the cell background threshold, the pixels were included in the data analysis. For each investigated loading concentration and time point, at least 120 cells in multiple areas were inspected, recorded, and analyzed. The relative scattering intensities (I_1, I_2, I_3) were calculated by integrating the intensities on the three wavelength channels (λ_1, λ_2, λ_3) for all selected pixels in all investigated cells and subsequent division by the sum of the total intensities of all three channels.

Cell Viability Measurements. After incubation of the cells with different concentrations of silver NPs for defined times, a commercial live/dead cell viability assay (Life Technologies, USA) was added to the cells according to the manufacturer's directions and maintained in the incubator for 30 min. Then the cells were washed with HBSS to remove the excess dye. The assay consists of two components: calcein acetoxymethyl (calcein AM) and ethidium homodimer-1 (EthD-1). Nonfluorescent cell−permeable calcein AM is converted to intensely fluorescent calcein by intracellular esterase in living cells, while EthD-1 enters cells with damaged membranes and produces a bright red fluorescence in dead cells. Living cells were detected with excitation and emission filters centered at 480 ± 17 and 510 ± 10 nm, respectively, and a 495 nm dichroic mirror. The EthD-1 signals for dead cells were measured with excitation and emission centered at 500 ± 25 and 610 ± 10 nm, respectively, and a 525 nm dichroic mirror.

Optical Correlation of NPs with Lysosome Tracker. LysoTracker Red DND-99 (Invitrogen) was employed to localize the acidic compartments. J774A.1 cells were first exposed to a prewarmed solution of 4.5 μg/mL silver NPs for 5 min in HBSS, after which unbound particles were washed away with copious amounts of prewarmed HBSS buffer. Subsequently the cells were cultured for another 24 h in nanoparticle-free culture medium before incubation with 1 μM LysoTracker Red solution for 0.5 h under growth conditions. The cell slides were washed and observed using a fluorescence microscope using an appropriate filter set (excitation: 563 ± 9 nm; emission: 600 ± 10 nm; 580 nm dichroic). Dark-field scattering images were recorded under white-light illumination as described.

Fluorescent Immunolabeling of the Surface Marker. J774A.1 cells were grown on glass coverslides to approximately 30% confluency. Cells were fixed by 2% formaldehyde solution for 15 min at room temperature followed by washing three times with ice-cold 1× PBS for 5 min each time. The cells were then incubated in ice-cold 1× PBS buffer containing 1% BSA for 1 h to block nonspecific binding at room temperature and subsequently washed three times with copious amounts of ice-cold 1× PBS buffer for 5 min. The cells were then incubated with monoclonal anti-F4/80 antibody conjugated with FITC (diluted 1:10 in 1× PBS) or monoclonal anti-CD14 antibody conjugated with FITC (diluted 1:10 in 1× PBS) in a water vapor saturated atmosphere for 2 h at room temperature. Finally the cell slides were washed three times with 1× PBS buffer for 5 min each time and then integrated into a homemade flow chamber and transferred to a combined dark-field and fluorescence microscope for inspection. The fluorescence signal was detected with excitation and emission filters centered at 480 ± 17 and 510 ± 10 nm, respectively, and a 495 nm dichroic mirror.

Conflict of Interest: The authors declare no competing financial interest.

Supporting Information Available: Figures S1−S4. This material is available free of charge *via* the Internet at http://pubs.acs.org.

Acknowledgment. This work was supported by the National Institutes of Health (NIH/NCI) through grant 5R01CA138509-04. We thank Dr. Todd Blute (Department of Biology, Boston University) for assisting with the TEM sample preparation.

REFERENCES AND NOTES

1. Balbus, J. M.; Maynard, A. D.; Colvin, V. L.; Castranova, V.; Daston, G. P.; Denison, R. A.; Dreher, K. L.; Goering, P. L.; Goldberg, A. M.; Kulinowski, K. M.; *et al*. Meeting Report: Hazard Assessment for Nanoparticles-Report from an Interdisciplinary Workshop. *Environ. Health Perspect.* **2007**, *115*, 1654–1659.
2. Oberdörster, G. Safety Assessment for Nanotechnology and Nanomedicine: Concepts of Nanotoxicology. *J. Intern. Med.* **2010**, *267*, 89–105.
3. Lewinski, N.; Colvin, V.; Drezek, R. Cytotoxicity of Nanoparticles. *Small* **2008**, *4*, 26–49.
4. Thubagere, A.; Reinhard, B. M. Nanoparticle-Induced Apoptosis Propagates through Hydrogen-Peroxide-Mediated Bystander Killing: Insights from a Human Intestinal Epithelium *in Vitro* Model. *ACS Nano* **2010**, *4*, 3611–3622.
5. Hume, D. A. The Mononuclear Phagocyte System. *Curr. Opin. Immunol.* **2006**, *18*, 49–53.
6. Gordon, S. Pattern Recognition Receptors: Doubling up for the Innate Immune Response. *Cell* **2002**, *111*, 927–930.
7. Haase, A. T., J.; Jungnickel, H.; Graf, P.; Mantion, A.; Draude, F.; Plendl, J.; Goetz, M. E.; Galla, A.; Masic, A.; Thünemann, A. F.; Taubert, A.; Arlinghaus, H. F.; Luch, A. Toxicity of Silver Nanoparticles in Human Macrophages: Uptake, Intracellular Distribution and Cellular Responses. *J. Phys.: Conf. Ser.* **2011**, *304*, 012030.
8. Carlson, C.; Hussain, S. M.; Schrand, A. M.; Braydich-Stolle, L. K.; Hess, K. L.; Jones, R. L.; Schlager, J. J. Unique Cellular Interaction of Silver Nanoparticles: Size-Dependent Generation of Reactive Oxygen Species. *J. Phys. Chem. B* **2008**, *112*, 13608–13619.
9. Park, J.; Lim, D.-H.; Lim, H.-J.; Kwon, T.; Choi, J.-s.; Jeong, S.; Choi, I.-H.; Cheon, J. Size Dependent Macrophage Responses and Toxicological Effects of Ag Nanoparticles. *Chem. Commun.* **2011**, *47*, 4382–4384.
10. Park, M. V. D. Z.; Neigh, A. M.; Vermeulen, J. P.; de la Fonteyne, L. J. J.; Verharen, H. W.; Briede, J. J.; van Loveren, H.; de Jong, W. H. The Effect of Particle Size on the Cytotoxicity, Inflammation, Developmental Toxicity and Genotoxicity of Silver Nanoparticles. *Biomaterials* **2011**, *32*, 9810–9817.
11. Johnston, H. J.; Hutchison, G.; Christensen, F. M.; Peters, S.; Hankin, S.; Stone, V. A Review of the *in Vivo* and *in Vitro* Toxicity of Silver and Gold Particulates: Particle Attributes and Biological Mechanisms Responsible for the Observed Toxicity. *Crit. Rev. Toxicol.* **2010**, *40*, 328–346.
12. Marambio-Jones, C.; Hoek, E. M. V. A Review of the Antibacterial Effects of Silver Nanomaterials and Potential Implications for Human Health and the Environment. *J. Nanopart. Res.* **2010**, *12*, 1531–1551.
13. Kim, S.; Oh, W.-K.; Jeong, Y. S.; Hong, J.-Y.; Cho, B.-R.; Hahn, J.-S.; Jang, J. Cytotoxicity of, and Innate Immune Response to, Size-Controlled Polypyrrole Nanoparticles in Mammalian Cells. *Biomaterials* **2011**, *32*, 2342–2350.
14. Yue, H.; Wei, W.; Yue, Z.; Lv, P.; Wang, L.; Ma, G.; Su, Z. Particle Size Affects the Cellular Response in Macrophages. *Eur. J. Pharm. Sci.* **2010**, *41*, 650–657.
15. Fernando, L. P.; Kandel, P. K.; Yu, J.; McNeill, J.; Ackroyd, P. C.; Christensen, K. A. Mechanism of Cellular Uptake of Highly Fluorescent Conjugated Polymer Nanoparticles. *Biomacromolecules* **2010**, *11*, 2675–2682.
16. Yen, H.-J.; Hsu, S.-h.; Tsai, C.-L. Cytotoxicity and Immunological Response of Gold and Silver Nanoparticles of Different Sizes. *Small* **2009**, *5*, 1553–1561.
17. Greaves, D. R.; Gordon, S. The Macrophage Scavenger Receptor at 30 Years of Age: Current Knowledge and Future Challenges. *J. Lipid Res.* **2009**, *50*, S282–S286.
18. Furumoto, K.; Nagayama, S.; Ogawara, K.; Takakura, Y.; Hashida, M.; Higaki, K.; Kimura, T. Hepatic Uptake of Negatively Charged Particles in Rats: Possible Involvement of Serum Proteins in Recognition by Scavenger Receptor. *J. Controlled Release* **2004**, *97*, 133–141.
19. Patel, P. C.; Giljohann, D. A.; Daniel, W. L.; Zheng, D.; Prigodich, A. E.; Mirkin, C. A. Scavenger Receptors Mediate Cellular Uptake of Polyvalent Oligonucleotide-Functionalized Gold Nanoparticles. *Bioconjugate Chem.* **2010**, *21*, 2250–2256.
20. Kanno, S.; Furuyama, A.; Hirano, S. A Murine Scavenger Receptor Marco Recognizes Polystyrene Nanoparticles. *Toxicol. Sci.* **2007**, *97*, 398–406.

21. Lunov, O.; Zablotskii, V.; Syrovets, T.; Rocker, C.; Tron, K.; Nienhaus, G. U.; Simmet, T. Modeling Receptor-Mediated Endocytosis of Polymer-Functionalized Iron Oxide Nanoparticles by Human Macrophages. *Biomaterials* **2011**, *32*, 547–555.
22. Kumari, S.; Swetha, M. G.; Mayor, S. Endocytosis Unplugged: Multiple Ways to Enter the Cell. *Cell Res.* **2010**, *20*, 256–275.
23. Doherty, G. J.; McMahon, H. T. Mechanisms of Endocytosis. *Annu. Rev. Biochem.* **2009**, *78*, 857–902.
24. Arnida; Janat-Amsbury, M. M.; Ray, A.; Peterson, C. M.; Ghandehari, H. Geometry and Surface Characteristics of Gold Nanoparticles Influence Their Biodistribution and Uptake by Macrophages. *Eur. J. Pharm. Biopharm.* **2011**, *77*, 417–423.
25. Skebo, J. E.; Grabinski, C. M.; Schrand, A. M.; Schlager, J. J.; Hussain, S. M. Assessment of Metal Nanoparticle Agglomeration, Uptake, and Interaction Using High-Illuminating System. *Int. J. Toxicol.* **2007**, *26*, 135–141.
26. Nel, A. E.; Maedler, L.; Velegol, D.; Xia, T.; Hoek, E. M. V.; Somasundaran, P.; Klaessig, F.; Castranova, V.; Thompson, M. Understanding Biophysicochemical Interactions at the Nano-Bio Interface. *Nat. Mater.* **2009**, *8*, 543–557.
27. Mahmoudi, M.; Lynch, I.; Ejtehadi, M. R.; Monopoli, M. P.; Bombelli, F. B.; Laurent, S. Protein-Nanoparticle Interactions: Opportunities and Challenges. *Chem. Rev.* **2011**, *111*, 5610–5637.
28. Sondi, I.; Salopek-Sondi, B. Silver Nanoparticles as Antimicrobial Agent: A Case Study on E-Coli as a Model for Gram-Negative Bacteria. *J. Colloid Interface Sci.* **2004**, *275*, 177–182.
29. Cho, K. H.; Park, J. E.; Osaka, T.; Park, S. G. The Study of Antimicrobial Activity and Preservative Effects of Nanosilver Ingredient. *Electrochim. Acta* **2005**, *51*, 956–960.
30. Morones, J. R.; Elechiguerra, J. L.; Camacho, A.; Holt, K.; Kouri, J. B.; Ramirez, J. T.; Yacaman, M. J. The Bactericidal Effect of Silver Nanoparticles. *Nanotechnology* **2005**, *16*, 2346–2353.
31. Ji, J. H.; Bae, G.-N.; Yun, S. H.; Jung, J. H.; Noh, H. S.; Kim, S. S. Evaluation of a Silver Nanoparticle Generator Using a Small Ceramic Heater for Inactivation of S. epidermidis Bioaerosols. *Aerosol Sci. Technol.* **2007**, *41*, 786–793.
32. Yguerabide, J.; Yguerabide, E. E. Light-Scattering Submicroscopic Particles as Highly Fluorescent Analogs and Their Use as Tracer Labels in Clinical and Biological Applications - I. Theory. *Anal. Biochem.* **1998**, *262*, 137–156.
33. Yguerabide, J.; Yguerabide, E. E. Light-Scattering Submicroscopic Particles as Highly Fluorescent Analogs and Their Use as Tracer Labels in Clinical and Biological Applications - II. Experimental Characterization. *Anal. Biochem.* **1998**, *262*, 157–176.
34. Schultz, S.; Smith, D. R.; Mock, J. J.; Schultz, D. A. Single-Target Molecule Detection with Nonbleaching Multicolor Optical Immunolabels. *Proc. Natl. Acad. Sci. U. S. A.* **2000**, *97*, 996–1001.
35. Kreibig, U.; Vollmer, M. *Optical Properties of Metal Clusters*; Springer: Berlin, 1995.
36. Yang, L.; Wang, H.; Yan, B.; Reinhard, B. M. Calibration of Silver Plasmon Rulers in the 1−25 nm Separation Range: Experimental Indications of Distinct Plasmon Coupling Regimes. *J. Phys. Chem. C* **2010**, *114*, 4901–4908.
37. Yan, B.; Boriskina, S. V.; Reinhard, B. M. Design and Implementation of Noble Metal Nanoparticle Cluster Arrays for Plasmon Enhanced Biosensing. *J. Phys. Chem. C* **2011**, *115*, 24437–24453.
38. Rong, G.; Wang, H.; Skewis, L. R.; Reinhard, B. M. Resolving Sub-Diffraction Limit Encounters in Nanoparticle Tracking Using Live Cell Plasmon Coupling Microscopy. *Nano Lett.* **2008**, *8*, 3386–3393.
39. Wang, J.; Boriskina, S. V.; Wang, H.; Reinhard, B. M. Illuminating Epidermal Growth Factor Receptor Densities on Filopodia through Plasmon Coupling. *ACS Nano* **2011**, *5*, 6619–6628.
40. Wang, H.; Rong, G.; Yan, B.; Yang, L.; Reinhard, B. M. Optical Sizing of Immunolabel Clusters through Multispectral Plasmon Coupling Microscopy. *Nano Lett.* **2011**, *11*, 498–504.
41. Aaron, J.; Travis, K.; Harrison, N.; Sokolov, K. Dynamic Imaging of Molecular Assemblies in Live Cells Based on Nanoparticle Plasmon Resonance Coupling. *Nano Lett.* **2009**, *9*, 3612–3618.
42. Crow, M. J.; Grant, G.; Provenzale, J. M.; Wax, A. Molecular Imaging and Quantitative Measurement of Epidermal Growth Factor Receptor Expression in Live Cancer Cells Using Immunolabeled Gold Nanoparticles. *Am. J. Roentgenol.* **2009**, *192*, 1021–1028.
43. Wang, J.; Yu, X.; Boriskina, S. V.; Reinhard, B. r. M. Quantification of Differential Erbb1 and Erbb2 Cell Surface Expression and Spatial Nanoclustering through Plasmon Coupling. *Nano Lett.* **2012**, *12*, 3231–3237.
44. Nordlander, P.; Oubre, C.; Prodan, E.; Li, K.; Stockman, M. I. Plasmon Hybridizaton in Nanoparticle Dimers. *Nano Lett.* **2004**, *4*, 899–903.
45. Rong, G.; Reinhard, B. M. Monitoring the Size and Lateral Dynamics of Erbb1 Enriched Membrane Domains through Live Cell Plasmon Coupling Microscopy. *PLoS One* **2012**, *7*, e34175.
46. Lundqvist, M.; Stigler, J.; Elia, G.; Lynch, I.; Cedervall, T.; Dawson, K. A. Nanoparticle Size and Surface Properties Determine the Protein Corona with Possible Implications for Biological Impacts. *Proc. Natl. Acad. Sci. U. S. A.* **2008**, *105*, 14265–14270.
47. Rice, P. J.; Kelley, J. L.; Kogan, G.; Ensley, H. E.; Kalbfleisch, J. H.; Browder, I. W.; Williams, D. L. Human Monocyte Scavenger Receptors Are Pattern Recognition Receptors for (1→3)-Beta-D-Glucans. *J. Leukocyte Biol.* **2002**, *72*, 140–146.
48. Aoyama, Y.; Kanamori, T.; Nakai, T.; Sasaki, T.; Horiuchi, S.; Sando, S.; Niidome, T. Artificial Viruses and Their Application to Gene Delivery. Size-Controlled Gene Coating with Glycocluster Nanoparticles. *J. Am. Chem. Soc.* **2003**, *125*, 3455–3457.
49. Nakai, T.; Kanamori, T.; Sando, S.; Aoyama, Y. Remarkably Size-Regulated Cell Invasion by Artificial Viruses. Saccharide-Dependent Self-Aggregation of Glycoviruses and Its Consequences in Glycoviral Gene Delivery. *J. Am. Chem. Soc.* **2003**, *125*, 8465–8475.
50. Osaki, F.; Kanamori, T.; Sando, S.; Sera, T.; Aoyama, Y. A Quantum Dot Conjugated Sugar Ball and Its Cellular Uptake on the Size Effects of Endocytosis in the Subviral Region. *J. Am. Chem. Soc.* **2004**, *126*, 6520–6521.
51. Gao, H. J.; Shi, W. D.; Freund, L. B. Mechanics of Receptor-Mediated Endocytosis. *Proc. Natl. Acad. Sci. U. S. A.* **2005**, *102*, 9469–9474.
52. Jiang, W.; Kim, B. Y. S.; Rutka, J. T.; Chan, W. C. W. Nanoparticle-Mediated Cellular Response Is Size-Dependent. *Nat. Nanotechnol.* **2008**, *3*, 145–150.
53. Zhang, S.; Li, J.; Lykotrafitis, G.; Bao, G.; Suresh, S. Size-Dependent Endocytosis of Nanoparticles. *Adv. Mater.* **2009**, *21*, 419–424.
54. Wang, S.-H.; Lee, C.-W.; Chiou, A.; Wei, P.-K. Size-Dependent Endocytosis of Gold Nanoparticles Studied by Three-Dimensional Mapping of Plasmonic Scattering Images. *J. Nanobiotechnol.* **2010**, 8.
55. Greulich, C.; Diendorf, J.; Simon, T.; Eggeler, G.; Epple, M.; Koeller, M. Uptake and Intracellular Distribution of Silver Nanoparticles in Human Mesenchymal Stem Cells. *Acta Biomater.* **2011**, *7*, 347–354.
56. Kittler, S.; Greulich, C.; Diendorf, J.; Koeller, M.; Epple, M. Toxicity of Silver Nanoparticles Increases during Storage Because of Slow Dissolution under Release of Silver Ions. *Chem. Mater.* **2010**, *22*, 4548–4554.
57. Greulich, C.; Kittler, S.; Epple, M.; Muhr, G.; Koeller, M. Studies on the Biocompatibility and the Interaction of Silver Nanoparticles with Human Mesenchymal Stem Cells (Hmscs). *Langenbecks Arch. Surg.* **2009**, *394*, 495–502.
58. Kaksonen, M.; Toret, C. P.; Drubin, D. G. Harnessing Actin Dynamics for Clathrin-Mediated Endocytosis. *Nat. Rev. Mol. Cell Biol.* **2006**, *7*, 404–414.

59. Merrifield, C. J.; Feldman, M. E.; Wan, L.; Almers, W. Imaging Actin and Dynamin Recruitment during Invagination of Single Clathrin-Coated Pits. *Nat. Cell Biol.* **2002**, *4*, 691–698.
60. Chamberlain, L. M.; Godek, M. L.; Gonzalez-Juarrero, M.; Grainger, D. W. Phenotypic Non-Equivalence of Murine (Monocyte-) Macrophage Cells in Biomaterial and Inflammatory Models. *J. Biomed. Mater. Res., Part A* **2009**, *88A*, 858–871.
61. Burke, B.; Lewis, C. E. *The Macrophage*; Oxford University Press: Oxford, U.K, 2002.
62. Gordon, S.; Taylor, P. R. Monocyte and Macrophage Heterogeneity. *Nat. Rev. Immunol.* **2005**, *5*, 953–964.
63. Godek, M. L.; Sampson, J. A.; Duchsherer, N. L.; Mcelwee, Q.; Grainger, D. W. Rho Gtpase Protein Expression and Activation in Murine Monocytes/Macrophages Are Not Modulated by Model Biomaterial Surfaces in Serum-Containing *in Vitro* Cultures. *J. Biomater. Sci., Polym. Ed.* **2006**, *17*, 1141–1158.
64. Godek, M. L.; Duchsherer, N. L.; McElwee, Q.; Grainger, D. W. Morphology and Growth of Murine Cell Lines on Model Biomaterials. *Biomed. Sci. Instrum.* **2004**, *40*, 7–12.
65. Daigneault, M.; Preston, J. A.; Marriott, H. M.; Whyte, M. K. B.; Dockrell, D. H. The Identification of Markers of Macrophage Differentiation in Pma-Stimulated Thp-1 Cells and Monocyte-Derived Macrophages. *PLoS One* **2010**, *5*, e8668.
66. Gordon, S.; Taylor, P. R. Monocyte and Macrophage Heterogeneity. *Nat. Rev. Immunol.* **2005**, *5*, 953–964.
67. Hirsch, S.; Austyn, J. M.; Gordon, S. Expression of the Macrophage-Specific Antigen F4-80 during Differentiation of Mouse Bone-Marrow Cells in Culture. *J. Exp. Med.* **1981**, *154*, 713–725.
68. McGilvray, I. D.; Serghides, L.; Kapus, A.; Rotstein, O. D.; Kain, K. C. Nonopsonic Monocyte/Macrophage Phagocytosis of Plasmodium Falciparum-Parasitized Erythrocytes: A Pole for Cd36 in Malarial Clearance. *Blood* **2000**, *96*, 3231–3240.
69. Speert, D. P.; Silverstein, S. C. Phagocytosis of Unopsonized Zymosan by Human Monocyte-Derived Macrophages - Maturation and Inhibition by Mannan. *J. Leukocyte Biol.* **1985**, *38*, 655–658.
70. Garcia-Garcia, E.; Rosales, R.; Rosales, C. Phosphatidylinositol 3-Kinase and Extracellular Signal-Regulated Kinase Are Recruited for Fc Receptor-Mediated Phagocytosis during Monocyte-to-Macrophage Differentiation. *J. Leukocyte Biol.* **2002**, *72*, 107–114.
71. Coller, S. P.; Paulnock, D. M. Signaling Pathways Initiated in Macrophages after Engagement of Type a Scavenger Receptors. *J. Leukocyte Biol.* **2001**, *70*, 142–148.
72. Atwood, W. J. A Combination of Low-Dose Chlorpromazine and Neutralizing Antibodies Inhibits the Spread of Jc Virus (Jcv) in a Tissue Culture Model: Implications for Prophylactic and Therapeutic Treatment of Progressive Multifocal Leukencephalopathy. *J. Neurovirol.* **2001**, *7*, 307–310.
73. Perry, D. G.; Daugherty, G. L.; Martin, W. J. Clathrin-Coated Pit-Associated Proteins Are Required for Alveolar Macrophage Phagocytosis. *J. Immunol.* **1999**, *162*, 380–386.
74. Hambleton, S.; Steinberg, S. P.; Gershon, M. D.; Gershon, A. A. Cholesterol Dependence of Varicella-Zoster Virion Entry into Target Cells. *J. Virol.* **2007**, *81*, 7548–7558.
75. Aoki, T.; Nomura, R.; Fujimoto, T. Tyrosine Phosphorylation of Caveolin-1 in the Endothelium. *Exp. Cell Res.* **1999**, *253*, 629–636.
76. Starling, D.; Duncan, R.; Lloyd, J. B. The Role of Microtubules in Pinocytosis - Inhibition of Fluid-Phase Pinocytosis in the Rat Visceral Yolk-Sac by Mitoplasic and Related Agents. *Cell Biol. Int. Rep.* **1983**, *7*, 593–602.
77. Mercer, J.; Helenius, A. Virus Entry by Macropinocytosis. *Nat. Cell Biol.* **2009**, *11*, 510–520.
78. Clague, M. J.; Thorpe, C.; Jones, A. T. Phosphatidylinositol 3-Kinase Regulation of Fluid-Phase Endocytosis. *FEBS Lett.* **1995**, *367*, 272–274.
79. Moller, W.; Nemoto, I.; Matsuzaki, T.; Hofer, T.; Heyder, J. Magnetic Phagosome Motion in J774a.1 Macrophages: Influence of Cytoskeletal Drugs. *Biophys. J.* **2000**, *79*, 720–730.